



## 1 Seasonal dynamics of the COS and CO<sub>2</sub> exchange of a managed 2 temperate grassland

3 Felix M. Spielmann<sup>1</sup>, Albin Hammerle<sup>1</sup>, Florian Kitz<sup>1</sup>, Katharina Gerdel<sup>1</sup>, Georg Wohlfahrt<sup>1</sup>

4 <sup>1</sup>Department of Ecology, University of Innsbruck, Innsbruck, 6020, Austria

5 Correspondence to: Georg Wohlfahrt (Georg.Wohlfahrt@uibk.ac.at)

6 **Abstract.** Gross primary productivity (GPP), the CO<sub>2</sub> uptake by means of photosynthesis, cannot be measured directly on  
7 ecosystem scale, but has to be inferred from proxies or models. One newly emerged proxy is the trace gas carbonyl sulfide  
8 (COS). COS diffuses into plant leaves in a fashion very similar to CO<sub>2</sub>, but is generally not emitted by plants. Laboratory  
9 studies on leaf level gas exchange have shown promising correlations between the leaf relative uptake (LRU) of COS to CO<sub>2</sub>  
10 under controlled conditions. However, *in situ* measurements including daily to seasonal environmental changes are required,  
11 to test the applicability of COS as a tracer for GPP at larger temporal scales. To this end, we conducted concurrent  
12 ecosystem scale CO<sub>2</sub> and COS flux measurements above an agriculturally managed temperate mountain grassland. We also  
13 determined the magnitude and variability of the soil COS exchange, which can affect the LRU on ecosystem level. The  
14 cutting and removal of the grass at the site had a major influence on the soil as well as the total exchange of COS. The  
15 grassland acted as a major sink for CO<sub>2</sub> and COS during periods of high leaf area. The sink strength decreased after the cuts  
16 and the grassland turned into a net source for CO<sub>2</sub> and COS on ecosystem level. The soil acted as a small sink for COS when  
17 the canopy was undisturbed, but also turned into a source after the cuts, which we linked to higher incident radiation hitting  
18 the soil surface. However, the soil contribution was not large enough to explain the COS emission on ecosystem level,  
19 hinting to an unknown COS source possibly related to dead plant matter degradation. Over the course of the season, we  
20 observed a concurrent decrease of CO<sub>2</sub> and COS uptake on ecosystem level. With the exception of the short periods after the  
21 cuts, the LRU under high light conditions was rather stable and indicates a high correlation between the COS flux and GPP  
22 across the growing season.

23

### 24 1 Introduction

25 Carbonyl sulfide (COS) is the most abundant sulfur-containing gas in the atmosphere with tropospheric mixing ratios of  
26 ~500 ppt. Within the atmosphere, COS acts as a greenhouse gas with a 724 times higher direct radiative forcing efficiency as  
27 CO<sub>2</sub> (Brühl et al., 2012). After reaching the stratosphere, it reacts to sulfur aerosols via oxidation and photolysis, hence  
28 contributing to the backscattering of solar radiation and having a cooling effect on Earth's atmosphere (Krysztofiak et al.,  
29 2015;Whelan et al., 2018). The intra-seasonal atmospheric COS mixing ratio follows the pattern of CO<sub>2</sub> as terrestrial  
30 vegetation acts as the largest known sink for both species (Montzka et al., 2007;Whelan et al., 2018;Le Quere et al., 2018).  
31 However, the summer drawdown for COS is 6 times stronger than for CO<sub>2</sub>, (Montzka et al., 2007) as COS is generally not  
32 emitted by plants like CO<sub>2</sub>, which is released in respiration processes.

33 The uptake of COS by plants is mostly mediated by the enzyme carbonic anhydrase (CA), but also photolytic enzymes like  
34 Ribulose-1,5-bisphosphate-carboxylase/-oxygenase (Rubisco) (Lorimer and Pierce, 1989). This in turn means that COS and  
35 CO<sub>2</sub> share a similar pathway into leaves through the boundary layer, the stomata and the cytosol, up to their reaction sites.  
36 Compared to CO<sub>2</sub>, COS is processed in a one-way reaction to H<sub>2</sub>S and CO<sub>2</sub> (Protoschill-Krebs and Kesselmeier, 1992;Notni  
37 et al., 2007) and therefore not released by plants (with the exception of severely stressed plants (Bloem et al., 2012;Gimeno  
38 et al., 2017)). That makes COS an interesting tracer for estimating the stomatal conductance and the gross uptake of CO<sub>2</sub>,



39 referred to as gross primary production (GPP), on ecosystem level (Asaf et al., 2013;Kooijmans et al., 2017;Kooijmans et al.,  
40 2019). However, to estimate GPP using COS, the relative uptake of COS to GPP deposition velocities (LRU) must be known  
41 beforehand (see Eq.1), so that GPP can be estimated on the basis of the COS flux.

$$42 LRU = \frac{F_{COS}}{\chi_{COS}} / \frac{F_{CO_2}}{\chi_{CO_2}} \quad (\text{Eq.1})$$

43  $F_{COS}$  is the COS leaf flux ( $\text{pmol m}^{-2} \text{s}^{-1}$ ),  $F_{CO_2}$  is the gross  $\text{CO}_2$  uptake on leaf level ( $\mu\text{mol m}^{-2} \text{s}^{-1}$ ) and  $\chi_{COS}$  and  $\chi_{CO_2}$  are the  
44 ambient COS and  $\text{CO}_2$  mixing ratios in ppt and ppm, respectively. Leaf level studies for  $C_3$  plants have estimated the LRU to  
45 be around 1.7 with the 95% confidence interval between 0.7 and 6.2 (Whelan et al., 2018;Seibt et al., 2010;Sandoval-Soto et  
46 al., 2005). The large spread of the LRU most likely originates from differences between plant species, for example, leaf  
47 structure and plant metabolism (Wohlfahrt et al., 2012;Seibt et al., 2010), which questions the applicability of the concept of  
48 LRU in real-world ecosystems under naturally varying environmental conditions. It is also known that the LRU is just stable  
49 under high light conditions, since the uptake of  $\text{CO}_2$  by means of photosynthesis is a light driven process, while CA is able to  
50 process COS independently of light conditions (Maseyk et al., 2014;Yang et al., 2018;Stimler et al., 2011). Any model of  
51 LRU should therefore reflect diurnal changes in light conditions. Kooijmans et al. (2019) recently discovered that the vapor  
52 pressure deficit (VPD) appears to have a stronger control on  $F_{COS}$  than on  $F_{CO_2}$ , in an evergreen needle forest. If generally  
53 true, this would add further variability to the LRU and complicating the application of COS to estimate GPP. Besides inter-  
54 specific differences in LRU, the question remains unanswered if the LRU is also susceptible to seasonal changes of  
55 ecosystems for example, changes in species composition or phenology, which would further complicate the application of  
56 COS in carbon cycle research. Maseyk et al. (2014) observed COS emissions on ecosystem scale over a winter wheat field  
57 going into senescence, indicating that potentially strong sources of COS could distort LRU.

58 Since CA and other enzymes known to emit or take up COS are also present in microorganisms (Ogawa et al., 2013;Seefeldt  
59 et al., 1995;Ensign, 1995;Smeulders et al., 2013;Whelan et al., 2018), recent studies have also quantified the contribution of  
60 soils to the COS ecosystem flux (Kooijmans et al., 2017;Spielmann et al., 2019;Maseyk et al., 2014). COS soil fluxes could  
61 modify the LRU on ecosystem level and hence inferred GPP, if they are substantial compared to COS canopy fluxes. Similar  
62 to the ecosystem fluxes, the soil fluxes could not only be prone to diurnal, but also seasonal changes, depending on the  
63 substrate availability, environmental conditions (e.g. soil temperature and moisture), substrate quality and quantity, and  
64 changes in composition of the microbial communities (Kitz et al., 2019;Meredith et al., 2019). Recent studies have also  
65 linked COS soil emissions to abiotic processes dependent on light and/or temperature (Whelan and Rhew, 2015;Kitz et al.,  
66 2019;Meredith et al., 2018).

67 The goal of our study was to provide new insights into the seasonal variability of COS fluxes on ecosystem, soil and canopy  
68 level. To this end, we conducted a 6-month campaign on a managed temperate mountain grassland, measuring ecosystem as  
69 well as soil COS fluxes. Since the grassland was cut four times during the campaign, we were able to observe multiple  
70 growing cycles and investigate the diel and seasonal changes of the COS fluxes and the LRU in this highly dynamic  
71 ecosystem. We hypothesize that (H1) the grassland, given its large  $\text{CO}_2$  uptake capacity (Wohlfahrt et al. 2008), is a major  
72 sink for COS and that the sink strength decreases over the course of the season, (H2) the drying of the cut grass leads to a  
73 release of COS, (H3) the LRU will change after the cuts, due to stressed plants and drying plant parts in the field, but is  
74 otherwise stable, (H4) the cuts turn the soil into a COS source, due to the larger amount of light reaching the soil surface  
75 (Kitz et al., 2017), but once a reasonably high leaf area index (LAI) has developed, COS is taken up by soil.



76 **2 Methods**

77 **2.1 Study site and period**

78 The study was conducted at an intensively managed mountain grassland in the municipal territory of Neustift (Austria) in  
79 Stubai valley (FLUXNET ID: AT-Neu; doi: [10.18140/FLX/1440121](https://doi.org/10.18140/FLX/1440121)). The grassland is situated at an elevation of 970 m a.s.l.  
80 in the middle of the flat valley bottom. The soil was classified as Fluvisol with an estimated depth of 1 m with the majority  
81 of roots located within the first 10 cm. Measurements were conducted between 01.05.2015 and 31.10.2015 (183 days). The  
82 vegetation was described as Pastinaco-Arrhenatheretum and consisted mainly of *Dactylis glomerata*, *Festuca pratensis*,  
83 *Alopecurus pratensis*, *Trisetum flavescens*, *Ranunculus acris*, *Taraxacum officinale*, *Trifolium repens*, *Trifolium pratense*,  
84 and *Carum carvi* (Kitz et al., 2017). During the campaign, the grassland was cut four times (02.06./07.07./21.08./01.10.2015)  
85 and the biomass left to dry on the field for up to one day, before being removed as silage. The field site was fertilized with  
86 organic manure at the end of the season (07.10.2015).

87 **2.2 Leaf area index**

88 The LAI was estimated from assessments of the average canopy height, which were related to destructive LAI  
89 measurements, using the following sigmoid function:

$$90 \quad LAI = \frac{1}{(1 + \exp(-(a_1 DOY + a_2)))(b_1 - b_2)} \quad (\text{Eq.2})$$

91 where DOY is the day of the year and a<sub>1</sub>, a<sub>2</sub>, b<sub>1</sub> and b<sub>2</sub> are factors that were optimized for each growing period, for  
92 example, before the first cut, between cuts and after fourth cut (Wohlfahrt et al., 2008). Additionally, biomass samples were  
93 taken at 15 occasions, to assist with the LAI calculation.

94 **2.3 Mixing ratio measurements**

95 The CO<sub>2</sub> ( $\chi_{\text{CO}_2}$ ) and COS ( $\chi_{\text{COS}}$ ) mixing ratios were measured using a Quantum Cascade Laser (QCL) Mini Monitor  
96 (Aerodyne Research, Billerica, MA, USA) at a wavenumber of ca. 2056 cm<sup>-1</sup> and at a frequency of 10 Hz. To minimize the  
97 effect of air temperature (T<sub>air</sub>) changes on the instrument, we placed it in an insulated box which in turn was located in a  
98 climate controlled instrument hut (30°C). The cooling of the laser was achieved by a chiller (ThermoCube 400, Solid State  
99 Cooling Systems, Wappinger Falls, NY, USA).

100 We used ¼ inch Teflon™ tubing, stainless steel fittings (SWAGELOK, Solon, OH, USA and FITOK, Offenbach, HE,  
101 Germany), Teflon Filters (Savilex, EdenPrairie, MN, USA) as well as COS-inert valves (Parker-Hannafin, Cleveland, OH,  
102 USA) to ensure that only materials known not to interact with COS were used for the measurement and calibration airflow.  
103 The H<sub>2</sub>O and CO<sub>2</sub> mixing ratios ( $\chi_{\text{H}_2\text{O}}$  &  $\chi_{\text{CO}_2}$ ) were measured by a closed-path infrared gas analyzer (IRGA) (Licor 6262,  
104 LICOR Biosciences, Lincoln, NE, USA). Since the data of the QCL, the sonic anemometer and the IRGA were saved on two  
105 separate PCs, a network time protocol software (NTP, Meinberg, NI, Germany) was used to keep the time on both devices  
106 synchronized. We corrected known  $\chi_{\text{COS}}$  drift issues of the QCL (Kooijmans et al., 2016) by doing half hourly calibrations  
107 for 1 min with a gas of known  $\chi_{\text{COS}}$ . The gas cylinders (working standards) used for the calibrations were either pressurized  
108 air (UN 1002) or nitrogen (UN 1066), which were cross-compared (when working standard cylinders were full and close to  
109 empty) to an Aculife-treated aluminum pressurized air cylinder obtained from the National Oceanic & Atmospheric  
110 Administration (NOAA). The latter was analyzed by the central calibration laboratory of NOAA for its  $\chi_{\text{COS}}$  using gas  
111 chromatography on 06.04.2015. We then linearly interpolated between the offsets of the half hourly calibrations and used the  
112 retrieved values to correct the high frequency COS data. Due to issues with the scale gas cylinder, no absolute concentrations  
113 were available before the first cut and therefore no LRU was calculated for this period.



114 **2.3.1 Mixing ratio measurements within the canopy**

115 In order to investigate the  $\chi_{\text{COS}}$  within the canopy, we used a multiplexer and 8  $\frac{1}{4}$  inch Teflon<sup>TM</sup> tubes to measure the  $\chi_{\text{COS}}$  at  
116 8 heights within and above the canopy i.e. at 2, 5, 10, 20, 30, 40, 50 & 250 cm height above ground with a tube length of  
117 15 m for each height. The upper two intakes were located at the eddy covariance measurement and canopy height,  
118 respectively. Each height was measured for 1 min at 1 Hz and  $2 \text{ l min}^{-1}$ , while the other lines were each flushed at  $2 \text{ l min}^{-1}$ .  
119 The  $\chi_{\text{COS}}$  drift was also corrected by doing half hourly calibrations (see section 2.3).

120

121 **2.4 COS soil fluxes**

122 **2.4.1 Soil chamber setup**

123 To quantify soil COS fluxes, we installed four stainless steel (SAE grade: 316L) rings 5 cm into the soil. They remained on  
124 site for 112 days (10.06.2015 – 30.09.2015). Two additional rings were installed on the 31.08.2015 and the 02.10.2015 to  
125 examine any long-term effects of the ring placement and to replace the original rings for the measurements in September and  
126 October. The aboveground biomass within each ring was removed at least one day prior to each measurement day. The roots  
127 within as well as the vegetation surrounding the rings were not removed and natural litter was left in place. At days without  
128 measurements the soil within the rings was covered by fleece to prevent it from drying out.

129 To measure the soil fluxes, a transparent fused silica-glass chamber (Kitz et al., 2017) was placed into the water filled  
130 channel of the steel rings, while air was sucked through the chamber to the QCL at a flow rate of  $1.5 \text{ l min}^{-1}$ . The chamber  
131  $\chi_{\text{COS}}$  was then compared with the ambient  $\chi_{\text{COS}}$  above the chamber, using a second inlet to which we switched before the  
132 chamber measurement and after reaching stable readings inside the chamber. Overall, 243 chamber measurements were  
133 conducted over the course of the campaign including day and nighttime measurements. Additional manual measurements  
134 included a hand-held sensor (WET-2, Delta-T Devices, Cambridge, England) to measure soil water content (SWC) and soil  
135 temperature ( $T_{\text{soil}}$ ) at a soil depth of 5 cm simultaneously with the soil chamber measurements next to the rings.

136 **2.4.1 COS soil flux calculation**

137 The COS soil flux was calculated using the following equation:

$$138 F = q(\chi_{\text{cos2}} - \chi_{\text{cos1}})/A \quad (\text{Eq.3})$$

139 where  $F$  is the COS soil flux ( $\text{pmol m}^{-2} \text{ s}^{-1}$ ),  $q$  denotes the flowrate in ( $\text{mol s}^{-1}$ ),  $\chi_{\text{cos2}}$  and  $\chi_{\text{cos1}}$  are the chamber and ambient  
140  $\chi_{\text{cos}}$  in ppt, respectively and  $A$  the soil surface area ( $0.032 \text{ m}^2$ ) covered by the chamber. A more detailed description can be  
141 found in Kitz et al. (2017).

142 **2.4.2 COS soil exchange modelling**

143 Due to the removal of the aboveground biomass and the consequent higher shortwave radiation reaching the soil surface in  
144 the chambers, compared to the soil below the canopy, we simulated the soil COS exchange for natural conditions. The soil  
145 flux was modelled using our measured soil fluxes and additionally retrieved soil and meteorological data -  $T_{\text{soil}}$ , soil water  
146 content (SWC) at 5 cm depth next to the chambers and incident shortwave radiation reaching the soil surface ( $R_{\text{SW-soil}}$ ) - as  
147 input for a random forest regression model (Liaw and Wiener, 2002). The soil fluxes were modelled on half hourly basis for  
148 the whole duration of the measurement campaign to calculate the COS canopy fluxes from the difference of the COS  
149 ecosystem and soil fluxes. To this end we used the scikit-learn (sklearn Ver. 0.19.1) package, the pandas library and the  
150 Python Software Distribution Anaconda (Ver. 5.2.0) in the command shell Ipython (Ver. 6.4.0) based on the Programming  
151 language Python (Ver. 3.3.5). We used the Beer-Lambert law to model  $R_{\text{SW-soil}}$  under undisturbed conditions as the  
152 aboveground vegetation was removed to measure the COS exchange of bare soil:



153  $R_{SW-soil} = R_{SW} \exp(-K LAI)$  (Eq.4)

154 where  $R_{SW-soil}$  ( $\text{Wm}^{-2}\text{s}^{-1}$ ) is the shortwave radiation (SW) reaching the soil surface,  $R_{SW}$  is the incoming SW radiation  
155 reaching the top of the canopy, LAI is the plant area index (Eq. 2) and K is the canopy extinction coefficient assuming a  
156 spherical leaf inclination distribution (Wohlfahrt et al., 2001), which was calculated using the following equation:

157  $K = \frac{1}{2\cos(\psi)}$  (Eq.5)

158 where  $\psi$  is the zenith angle of the sun in radians.

159

160 A random forest with 1000 trees was grown which resulted in an out of bag (OOB) score of (0.82). The optimal input  
161 parameters, including maximum tree depth, were determined with the function GridSearchCV from the sklearn package.

## 162 2.5 Ecosystem fluxes

### 163 2.5.1 Setup for ecosystem fluxes

164 The COS,  $\text{CO}_2$  and  $\text{H}_2\text{O}$  ecosystem fluxes were obtained using the eddy covariance method (Aubinet et al., 1999; Baldocchi,  
165 2014). We used a 3-axis sonic anemometer (Gill R3IA, Gill Instruments Limited, Lymington, UK) to obtain-high resolution  
166 data of the 3 wind components. The intake of the tube for the eddy covariance measurements was installed in close  
167 proximity to the sonic anemometer and insulated as well as heated above  $T_{air}$  to prevent condensation within the tube. The air  
168 was sucked to the QCL at a flowrate of  $7 \text{ l min}^{-1}$  using a Vacuum Pump (Agilent Technologies, CA, USA).

### 169 2.5.2 Ecosystem flux calculation

170 In a first step we used a self-developed software to determine the time lag, introduced by the separation of tube intake and  
171 the sonic anemometer and the tube length, between the QCL and sonic dataset (Hortnagl et al., 2010). The data were then  
172 processed using the software EdiRe (University of Edinburgh, UK) and Matlab2019a (MathWorks, MA, USA). We used the  
173 laser drift corrected  $\chi_{\text{COS}}$  data and linear detrending to process the data before following the procedure to correct for sensor  
174 response, tube attenuation, path averaging and sensor separation following Gerdel et al. (2017). The random flux uncertainty  
175 was calculated following Langford et al. (2015).

176 We estimated the COS canopy flux from the difference between the measured COS ecosystem and the modelled COS soil  
177 flux.

### 178 2.5.3 Flux partitioning and leaf relative uptake

179 The GPP on ecosystem level was determined using the FP+ model put forward by Spielmann et al. (2019). The model  
180 estimates the GPP on the basis of nighttime net ecosystem exchange (NEE) measurements of  $\text{CO}_2$  that are assumed to  
181 provide the temperature response of the ecosystem respiration (RECO) as well as a light dependency curve to estimate GPP  
182 based on the daytime NEE (Lasslop et al., 2010):

183  $NEE = \frac{\alpha\beta R_{PAR}}{\alpha R_{PAR} + \beta} + rb e^{\frac{E_0}{T_{ref}-T_0} - \frac{1}{T_{air}-T_0}}$  (Eq.6)

184 where  $\alpha$  denotes the canopy light utilization efficiency ( $\mu\text{mol CO}_2 \mu\text{mol}^{-1}$  photons),  $\beta$  the maximum  $\text{CO}_2$  uptake rate of the  
185 canopy at light saturation ( $\mu\text{mol CO}_2 \text{ m}^{-2} \text{ s}^{-1}$ ),  $R_{PAR}$  the incoming photosynthetic active radiation ( $\mu\text{mol m}^{-2} \text{ s}^{-1}$ ),  $rb$  the  
186 ecosystem base respiration ( $\mu\text{mol m}^{-2} \text{ s}^{-1}$ ) at the reference temperature  $T_{ref}$  ( $^{\circ}\text{C}$ ), which is set to  $15^{\circ}\text{C}$ ,  $T_{air}$  ( $^{\circ}\text{C}$ ) refers to the  
187 air temperature and  $E_0$  ( $^{\circ}\text{C}$ ) to the temperature sensitivity of RECO.  $T_0$  was kept constant at  $-46.02^{\circ}\text{C}$ . We did not use the  
188 VPD modifier of beta put forward by Lasslop et al. (2010) as its value could not be estimated with confidence.

189 The FP+ model by Spielmann et al. (2019) extends the daytime FP (Eq.6) to also estimate the COS ecosystem fluxes by  
190 linking the GPP resulting from the first part on the right-hand side of Eq.6 with the COS exchange through:



$$191 \quad F_{COSmodel} = \frac{GPP LRU}{\chi_{CO_2}} / \chi_{cos} \quad (\text{Eq.7})$$

192 where  $F_{COSmodel}$  is the modelled COS flux ( $\text{pmol m}^{-2} \text{s}^{-1}$ ),  $\chi_{cos}$  (ppt) and  $\chi_{CO_2}$  (ppm) are the measured ambient mixing ratios of  
 193 COS and  $\text{CO}_2$  respectively and LRU (-) is the leaf relative uptake rate:

$$194 \quad LRU = \iota e^{\frac{\kappa}{R_{PAR}}} \quad (\text{Eq.8})$$

195 where  $\iota$  (-) corresponds to the LRU at high light intensity and the parameter  $\kappa$  ( $\mu\text{mol m}^{-2} \text{s}^{-1}$ ) governs the increase of LRU at  
 196 low light conditions. The light dependency of LRU originates from the fact that the COS uptake by the enzyme CA is light-  
 197 independent, while the  $\text{CO}_2$  uptake by Rubisco depends on solar radiation absorbed by leaf chlorophyll (Whelan et al.,  
 198 2018;Kooijmans et al., 2019;Wohlfahrt et al., 2012). We determined the parameter  $E_0$  by using nighttime data minimizing  
 199 the root squared mean error. For the determination of the remaining five unknown model parameters of the two flux  
 200 partitioning models we used DREAM, a multi-chain Markov Chain Monte Carlo algorithm (for more detail see Spielmann et  
 201 al. (2019)). We calculated the parameters for ~15 day windows but adjusted them to not overlap with a cut of the grassland.  
 202 The ecosystem relative uptake (ERU) was calculated using Eq. 1 substituting the GPP with the NEE and using the COS  
 203 ecosystem flux for  $F_{cos}$ .

#### 204 2.5.4 Linear perturbation analysis

205 The relative contribution of the parameters GPP,  $F_{COSmodel}$ ,  $\chi_{CO_2}$  and  $\chi_{cos}$  that drive  $\iota$  (Eq. 7) were estimated through a linear  
 206 perturbation analysis (Stoy et al., 2006).

207 The changes in  $\iota$  ( $\delta\iota$ ) between the target and the reference window (before the 2<sup>nd</sup> cut, i.e. 18.06.2015-07.07.2015) are  
 208 considered the total derivative of Eq. 7 and can be represented by a multivariate Taylors's expansion where the higher-order  
 209 terms are neglected in this first-order analysis:

$$210 \quad \delta\iota = \frac{\partial\iota}{\partial F_{COSmod}} dF_{cosmod} + \frac{\partial\iota}{\partial \chi_{cos}} d\chi_{cos} + \frac{\partial\iota}{\partial GPP} dGPP + \frac{\partial\iota}{\partial \chi_{CO_2}} d\chi_{CO_2} \quad (\text{Eq.9})$$

211 The relative contributions of the parameters were determined by computing the partial derivatives of Eq. 7.

$$212 \quad \frac{\partial\iota}{\partial F_{COSmod}} = \frac{\chi_{CO_2}}{\chi_{cos} GPP} \quad (\text{Eq.10})$$

$$213 \quad \frac{\partial\iota}{\partial \chi_{cos}} = \frac{-\chi_{CO_2} F_{COSmod}}{\chi_{cos}^2 GPP} \quad (\text{Eq.11})$$

$$214 \quad \frac{\partial\iota}{\partial GPP} = \frac{\chi_{CO_2} F_{COSmod}}{\chi_{cos} GPP^2} \quad (\text{Eq.12})$$

$$215 \quad \frac{\partial\iota}{\partial \chi_{CO_2}} = \frac{F_{COSmod}}{\chi_{cos} GPP} \quad (\text{Eq.13})$$

216

#### 217 2.6 Ancillary data

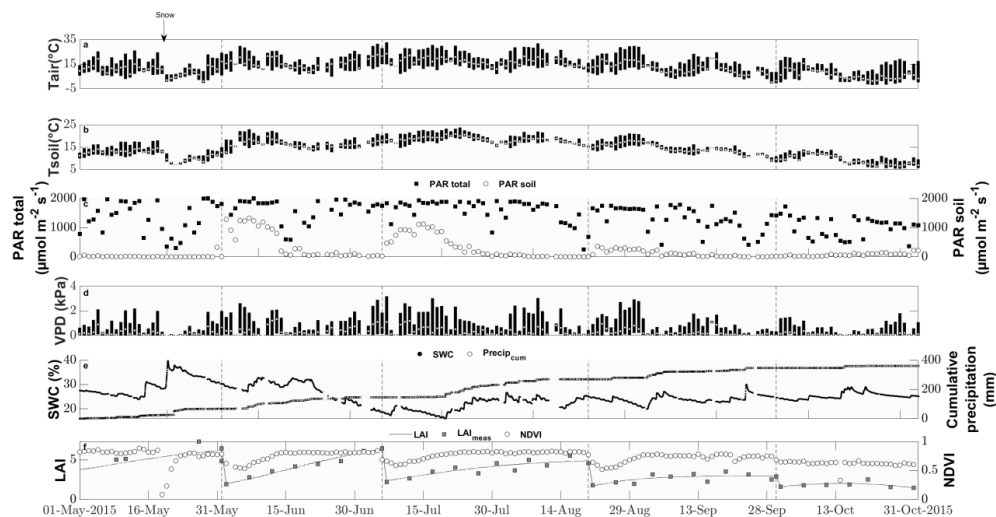
218 Supporting meteorological measurements included  $T_{air}$  (RFT-2, UMS, Munich, GER),  $T_{soil}$  (TCAV, Campbell Scientific,  
 219 Logan, UT, USA), SWC (ML2x, Delta-T Devices, Cambridge, UK), incident solar radiation (CNR-1, Klipp and Zonen,  
 220 Delft, NLD), incident photosynthetic active radiation (PAR) (BF2H, Delta-T Devices Ltd, Cambridge, UK) and the  
 221 Normalized Difference Vegetation Index (NDVI) sensor (SRS-NDVI, Meter, Pullman, WA, USA). The data were recorded  
 222 throughout the whole season as 1 min values and stored as half-hourly means and standard deviations.



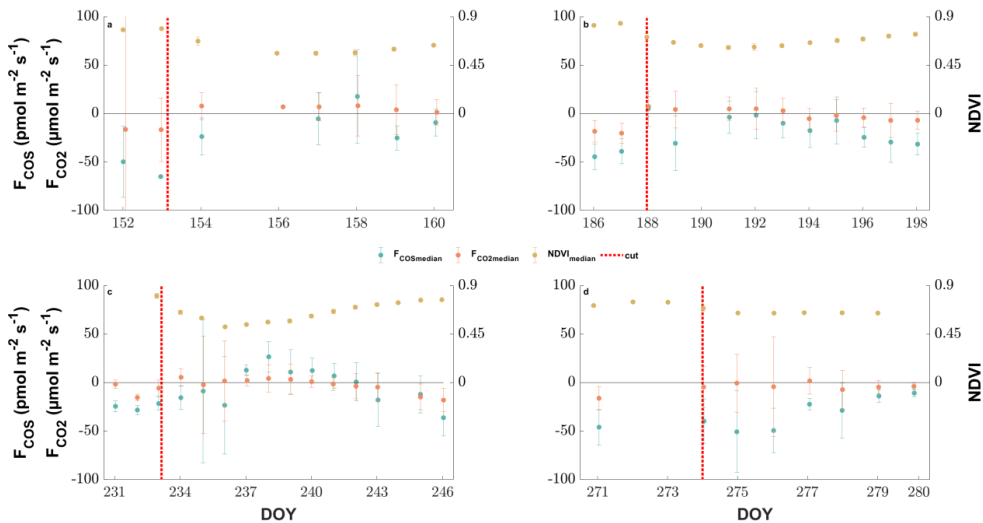
## 223 3 Results

### 224 3.1 Environmental conditions

225 Air temperature ranged between -2 °C and 33 °C with a mean of 13 °C during the study period from 15<sup>th</sup> of May to first of  
226 November (Fig. 1). While the majority of precipitation (total 360.5 mm) fell as rain, we observed an exceptionally late snow  
227 event on the 20<sup>th</sup> of May, which did not melt for almost two days (Fig. 1). Although the VPD reached values of above 2 kPa  
228 during 25 days, and plant available water dropped below 38 % on 21 days during the campaign (Fig. 1), we did not observe  
229 any relationship with COS (see Fig S1-S2). Due to the removal of the aboveground biomass, the cuts reduced LAI. They  
230 also reduced the normalized difference vegetation index (NDVI) (Fig. 1), which further decreased in the subsequent days as  
231 a consequence of dying plant parts remaining at the field site (Fig 2 panels a-c). This can also be observed in the webcam  
232 photos (**Photo S1-S3**).



233  
234 **Figure 1.** Seasonal cycle of ancillary variables. Daily minimum, maximum and median (a) air and (b) soil temperatures (°C) indicated by  
235 the lower and upper end of the bars and the white circle, respectively. (c) Daily maximum incident photosynthetic active radiation (μmol  
236 m<sup>-2</sup> s<sup>-1</sup>) reaching the top of the canopy (black squares) and reaching the soil surface (white circles). (d) Daily minimum, maximum and  
237 median vapor pressure deficit (kPa) indicated by the lower and upper end of the bars and the white circle, respectively. (e) Soil water  
238 content (%) depicted by black squares and cumulative precipitation (mm) depicted by open circles. (f) Modelled leaf area index (black  
239 lines), measured LAI (grey squares) and normalized difference vegetation index (open circles).



240

241 **Figure 2:** The response of the daily midday medians of NDVI (yellow circles), COS (blue circles) and CO<sub>2</sub> (red circles) ecosystem fluxes  
 242 around the 4 cutting events (a-d) of the grassland. The errorbars depict the respective median absolute deviations. The cuts are marked by a  
 243 red dashed line.

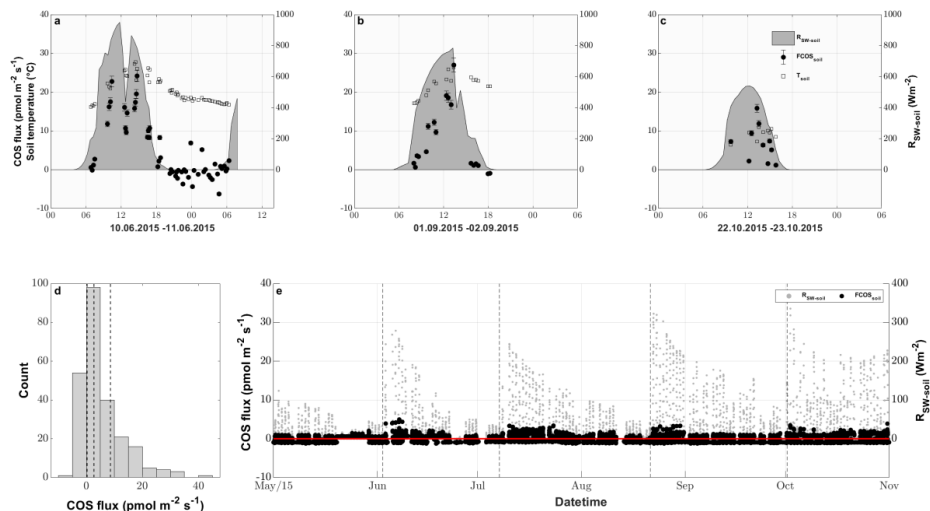
244

## 245 3.2 COS soil flux

246 The fluxes resulting from the soil chamber measurements ranged from -6.3 to 40.9 pmol m<sup>-2</sup>s<sup>-1</sup>, with positive fluxes denoting  
 247 emission (see Fig. 3 panel d).

248 During nighttime ( $R_{SW} = 0$ ,  $n = 43$ ), the soils of the grassland acted as a net sink for COS 74.4 % of the time (range of -4.4 to  
 249 6.9 pmol m<sup>-2</sup>s<sup>-1</sup>), whereas soils transitioned to a source in 88.5 % of all daytime measurements ( $R_{SW} > 0$ ,  $n = 200$ ), reaching  
 250 the highest fluxes of 40.9 pmol m<sup>-2</sup>s<sup>-1</sup> during midday (see Fig. 3 a-c and Fig. S3). This diel pattern was maintained over the  
 251 course of the season, however with decreasing maximum COS source strength of the soil towards the end of the season (Fig.  
 252 3 a-c and Fig. S3). The random forest regression revealed that the most important variable for predicting the soil fluxes was  
 253 the incident shortwave radiation reaching the soil surface ( $R_{SW-soil}$ ), accounting for more than 73.53 % of the total variance  
 254 explained by the final model, while SWC and  $T_{soil}$  only accounted for 17.84 % and 8.62 %, respectively. The fast response of  
 255 the COS soil fluxes to changes in  $R_{SW}$  can be seen in Fig. 3 a, where we observed a decrease of  $R_{SW-soil}$  as well as the COS  
 256 soil flux during a cloudy period, even when the soil temperature still increased. Soil fluxes estimated with the random forest  
 257 regression ranged from -1.3 to 5.0 pmol m<sup>-2</sup>s<sup>-1</sup>, reflecting the fact that under real-world conditions very little solar radiation  
 258 reaches the soil surface. (Fig. 3 e). The resulting emissions peaked during daytime shortly after the cuts when a high  
 259 proportion of incident radiation was reaching the soil surface, while simulated nighttime fluxes were dominated by uptake  
 260 (in 93 % of all cases) for the whole season.

261



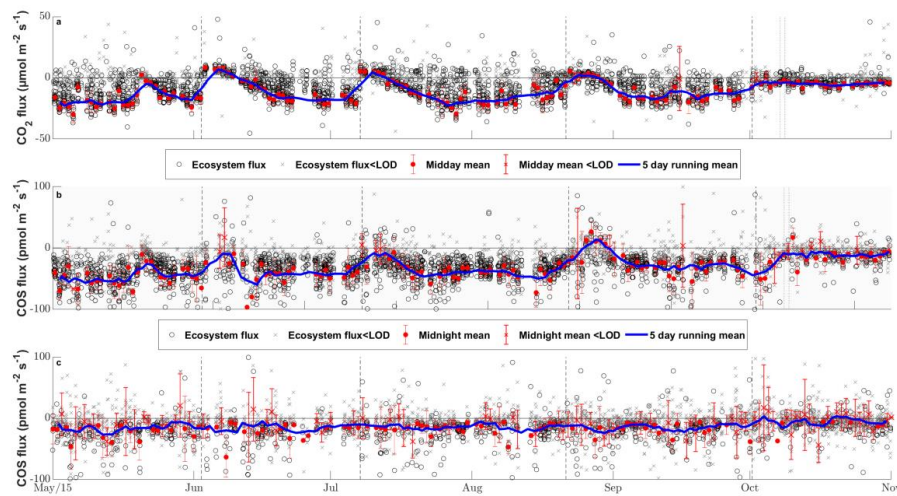
262

263 **Figure 3.** COS soil fluxes ( $\text{pmol m}^{-2} \text{s}^{-1}$ ) originating from manual chamber measurements of three selected days (a), (b) and (c) depicted by  
 264 black circles and open diamonds, respectively, incident shortwave radiation reaching the soil ( $R_{\text{SW-soil}}$ ) depicted by the gray area and soil  
 265 temperature ( $T_{\text{soil}}$ ) depicted by empty black bordered squares. (d) Histogram of all conducted COS soil chamber observations with the  
 266 dashed vertical lines depicting the 25., 50 and 75% quantile. (e) Season plot of the modelled COS soil fluxes ( $F_{\text{COS-soil}}$ ) depicted by the black  
 267 circles, incident shortwave radiation reaching the soil surface ( $R_{\text{SW-soil}}$ ) depicted by grey circles and the black dashed lines depicting the  
 268 cuttings of the grassland.

269

### 270 3.3 COS and CO<sub>2</sub> ecosystem-scale fluxes

271 The grassland acted as a net sink for COS during the majority of our study period with 80 % of the COS ecosystem fluxes  
 272 between -60.2  $\text{pmol m}^{-2} \text{s}^{-1}$  and -12.5  $\text{pmol m}^{-2} \text{s}^{-1}$  during daytime and -41.5  $\text{pmol m}^{-2} \text{s}^{-1}$  and -4.6  $\text{pmol m}^{-2} \text{s}^{-1}$  during nighttime.  
 273 However, we also observed a net release of COS at the field site 4.5 % of the time. The net CO<sub>2</sub> fluxes ranged from -20.7 to  
 274 3.2  $\mu\text{mol m}^{-2} \text{s}^{-1}$  and 1.6 to 28.7  $\mu\text{mol m}^{-2} \text{s}^{-1}$  for 80% of all observation during day and nighttime, with daytime net emissions  
 275 occurring after the cuttings of the grassland (Fig. 2 a-c and Fig. 4 a). While the COS nighttime fluxes remained unaffected by  
 276 the cuts (Fig. 4 c), the daytime fluxes showed a high variability (see Fig. 4 b). Especially after the cuts we observed a strong  
 277 decline in COS uptake and even times where the grassland turned into a net source for COS with midday means of up to 24.5  
 278  $\text{pmol m}^{-2} \text{s}^{-1}$  (Fig. 4 b) for up to 8 days after the cut, when the dried litter had already been removed (Fig. 2 a-c). Compared to  
 279 respiration processes outpacing GPP almost instantaneously after the cuts, the grassland reached its peak COS emission on  
 280 the day of the cut only in July, whereas the peak was reached five days after the cut in June and August (Fig. 2 a-c). The cut  
 281 in October led to a reduction in COS uptake, which was lowest three days after the cut (Fig. 2 d). After the fertilization of the  
 282 field in October the grassland also turned into a source for COS during midday hours for one day (Fig. 4 b). Our flux  
 283 measurements also included a time when the grassland was covered with snow (on the 20.05.2015), which reduced the COS  
 284 (and CO<sub>2</sub>) fluxes to values close to zero. Over the course of the season, we observed a decline in the magnitude of the  
 285 daytime COS uptake from  $-50.9 \pm 25.0 \text{ pmol m}^{-2} \text{s}^{-1}$  during midday in the first week of May down to  $-29.6 \pm 25.5 \text{ pmol m}^{-2} \text{s}^{-1}$   
 286 in the last week of October, which was also correlated with the decline in sink strength and shift to net emission of CO<sub>2</sub> from  
 287  $-19.9 \pm 8.0 \text{ pmol m}^{-2} \text{s}^{-1}$  to  $11.9 \pm 36.9 \mu\text{mol m}^{-2} \text{s}^{-1}$  (Fig. 4 c). We observed an increase in COS and CO<sub>2</sub> fluxes within the  
 288 growing phases after the cuts only up to an LAI of ~ 4 (-) (Fig. S4-S5), which then levelled out for COS and declined for  
 289 CO<sub>2</sub> due to ecosystem respiration compensating GPP.



290

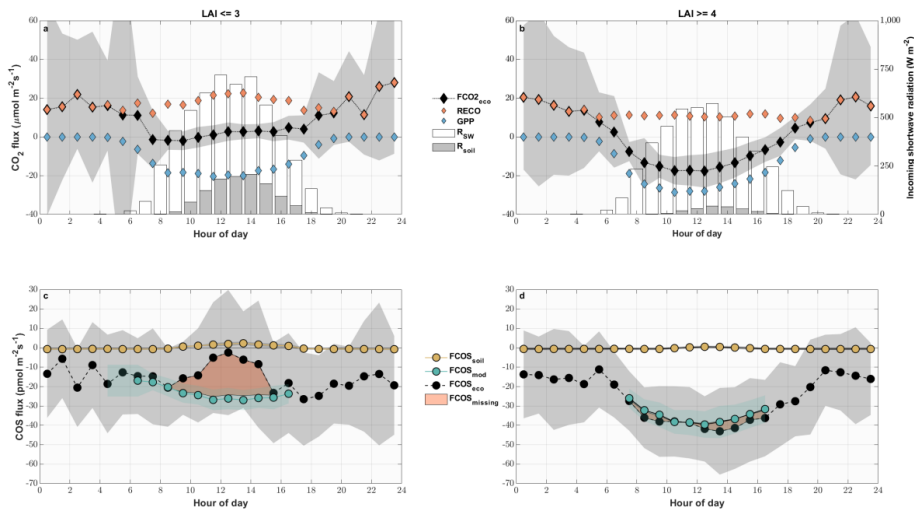
291 **Figure 4:** Seasonal cycle of the half hourly CO<sub>2</sub> (a), COS daytime (b) and COS nighttime (c) ecosystem fluxes in  $\mu\text{mol m}^{-2}\text{s}^{-1}$  and  $\text{pmol m}^{-2}\text{s}^{-1}$  depicted by black circles if they are above the limit of detection (LOD) and grey x's if they are below (Langford et al., 2015). The red 292 circles depict the mean fluxes between 11 a.m. and 2 p.m. CET for (a & b) and between 11 p.m. and 2 a.m. for (c) that are above the LOD, 293 while the red x's indicate means below the LOD. The red error bars depict the  $\pm 1$  standard deviation of the mean. The blue lines depict the 294 running mean (5 days) for the mean fluxes. The black dashed lines depict the cuttings of the grassland. 295

296

297 The seasonal pattern of a decrease in COS sink strength was similar for nighttime fluxes ( $-18.1 \pm 29.7 \text{ pmol m}^{-2}\text{s}^{-1}$  to  $-13.0 \pm$   
298  $22.5 \text{ pmol m}^{-2}\text{s}^{-1}$ ) (Fig. 4a). The mean nighttime respiration also decreased over the course of the season from  $15.9 \pm 28 \text{ pmol}$   
299  $\text{m}^{-2}\text{s}^{-1}$  to  $12.9 \pm 31.7 \text{ pmol m}^{-2}\text{s}^{-1}$  between May and October.

300 Periods of low (after cuts) and high (before cuts) LAI were compared as diel courses (Fig. 5). Over the course of the day,  
301 both periods were characterized by a mean uptake of COS (Fig 5 c & d). Even though the uptake was similar during  
302 nighttime, the daytime pattern differed considerably. The modelled contribution of the soil to the ecosystem scale COS flux  
303 under high LAI conditions (Fig. 5 d) was minor, contributing between 1 % and 5.5 % of the ecosystem flux during midday  
304 and morning/evening, respectively. In contrast, during low LAI conditions the soil contribution to the ecosystem fluxes  
305 increased during daytime and contributed up to 80.5% of the mean hourly COS ecosystem flux (Fig 5. c). While the  
306 grassland acted as a stronger sink for COS during daytime at a high LAI, reaching peak mean uptake values of up to  $-41.8$   
307  $\text{pmol m}^{-2}\text{s}^{-1} \pm 16.8 \text{ pmol m}^{-2}\text{s}^{-1}$  during midday, the mean daytime sink strength weakened and we observed close to zero  
308 fluxes during midday in periods of low LAI. The magnitude of the soil flux ( $2 \pm 1 \text{ pmol m}^{-2}\text{s}^{-1}$ ) was not high enough to  
309 explain the difference variation of up to  $-23.7 \text{ pmol m}^{-2}\text{s}^{-1}$  between the measured COS ecosystem flux and COS flux resulting  
310 from the FP+ model (Fig 5 c), suggesting a missing COS source. For phases of high LAI we saw a good agreement between  
311 modelled and measured COS ecosystem fluxes (Fig 5 d). While the grassland acted as a net sink for CO<sub>2</sub> during periods of  
312 high LAI (Fig. 5 b), a combination of a decline in GPP and an increase in RECO turned it into a net source during midday in  
313 periods of low LAI (Fig. 5 a).

314



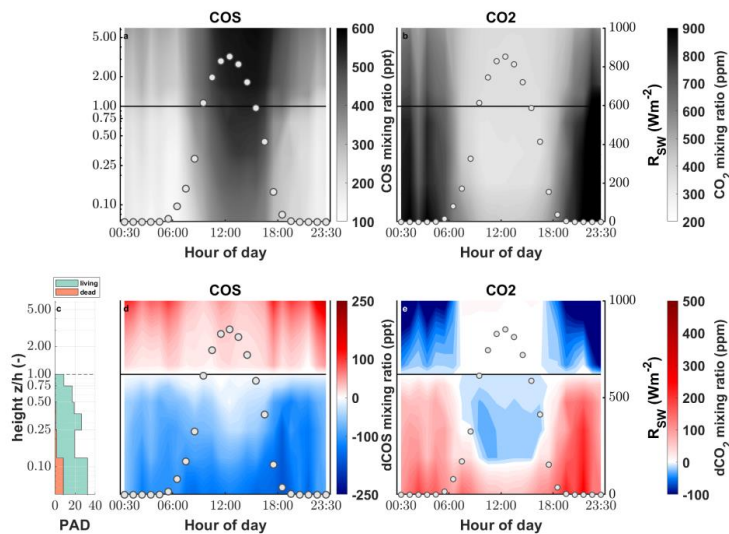
315

316 **Figure 5.** Mean diel variation of the measured and modelled CO<sub>2</sub> (a & b) and COS (c & d) fluxes for phases of low (LAI  $\leq 3$ ) (a & c) and  
 317 high (LAI  $\geq 4$ ) (b & d). The carats depict the modelled gross primary productivity (blue), the modelled ecosystem respiration (red) and  
 318 the measured CO<sub>2</sub> ecosystem fluxes (black) in  $\mu\text{mol m}^{-2}\text{s}^{-1}$ . The circles depict the modelled COS soil flux (yellow), the modelled COS  
 319 ecosystem flux (turquoise) and the measured CO<sub>2</sub> ecosystem fluxes (black) in  $\text{pmol m}^{-2}\text{s}^{-1}$ . The red area depicts the difference between the  
 320 measured ecosystem flux and the sum of the modelled fluxes. The grey areas depict the  $\pm 1$  standard deviation of the mean for all the  
 321 measured fluxes. The white bars depict the diel mean total incoming shortwave radiation ( $\text{W m}^{-2}\text{s}^{-1}$ ) while the grey bars indicate the diel  
 322 mean shortwave radiation reaching the soil surface.

323

### 324 3.4 COS mixing ratios above and within the canopy

325 While the canopy depleted the ambient  $\chi_{\text{COS}}$  during day as well as nighttime, we found that the  $\chi_{\text{COS}}$  reached values as low as  
 326 134 ppt (depletion of 102 ppt with respect to the mixing ratio at canopy height) during nighttime (see Fig. 6) at the bottom of  
 327 the canopy in contrast to the midday  $\chi_{\text{COS}}$ , which only went down to 389 ppt (depletion of 125 ppt with respect to the mixing  
 328 ratio at canopy height). We observed a decrease in  $\chi_{\text{CO}_2}$  (up to 26 ppm) within the most upper layers of the canopy compared  
 329 to  $\chi_{\text{CO}_2}$  at canopy height during daytime, while  $\chi_{\text{CO}_2}$  increased within the lowest layers compared to  $\chi_{\text{CO}_2}$  at the canopy height  
 330 due to soil respiration. The above canopy  $\chi_{\text{COS}}$  increased considerably starting at the onset of the day and reached 587 ppt at  
 331 16:00. Over the course of the season the midday ambient  $\chi_{\text{COS}}$  decreased from  $500 \pm 28$  ppt from mid-June to mid-July to  
 332  $405 \pm 29$  ppt in October with the trend of increasing  $\chi_{\text{COS}}$  starting at the end of September (see Fig. S6).



333

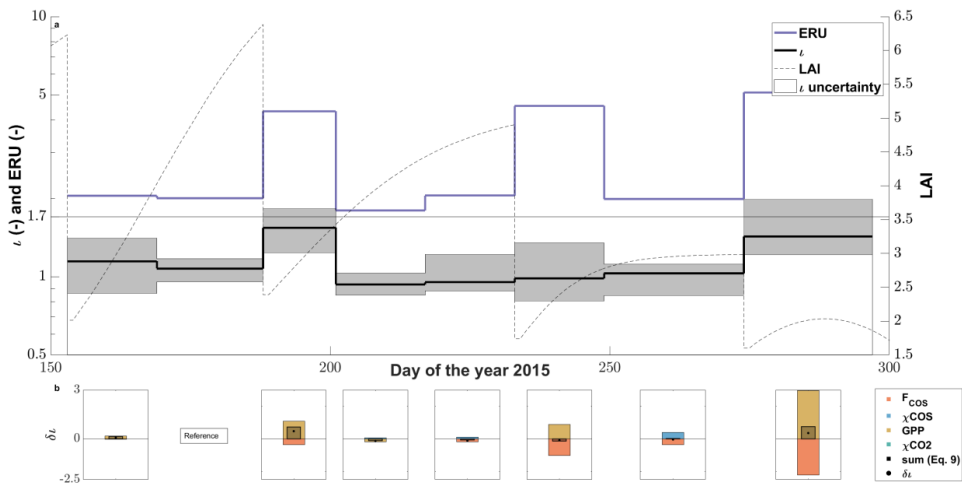
334 **Figure 6.** Vertical gradient of the (a) COS and (b) CO<sub>2</sub> mixing ratio (ppt and ppm, respectively) depicted by the background color between  
335 the soil and the eddy covariance tower at 250 cm for one day. The left y axis shows the log of the measurement divided by the canopy  
336 height (z/h). The white circles depict the incoming shortwave radiation ( $R_{SW}$ ) in ( $\text{W m}^{-2}\text{s}^{-1}$ ). Plant area density (PAD) split into living  
337 (green) and dead (brown) plant material (c). Vertical gradient of the difference between the mixing ratio at canopy height and each  
338 measurement height for (d) COS and (e) CO<sub>2</sub>.

339

### 340 3.5 Leaf and ecosystem relative uptake

341 The LRU at high-light conditions,  $\iota$ , which we calculated using the FP+ algorithm increased from relatively stable precut  
342 levels of 0.9–1.1 (–) after the 2<sup>nd</sup> and the 4<sup>th</sup> cut to up to 1.5 (–) (Fig. 7a). After the decrease in  $\iota$  between the 2<sup>nd</sup> and the 3<sup>rd</sup>  
343 cut,  $\iota$  increased steadily until the 4<sup>th</sup> cut, with the 3<sup>rd</sup> cut seemingly not having an effect. The reason for the increase in  $\iota$  after  
344 the 2<sup>nd</sup> and 4<sup>th</sup> cut was a stronger decrease in GPP than the COS uptake, while both decreased more evenly after the 3<sup>rd</sup> cut  
345 (Fig. 7b). We observed  $\iota$  in the period before the 4<sup>th</sup> cut to be influenced not only by a decrease in COS uptake, but also by a  
346 decrease in COS mixing ratio (Fig. 7b). The mean midday ERUs varied between  $1.9 \pm 0.1$  (–) before and  $4.6 \pm 0.3$  (–) after the  
347 cuts when excluding and  $3.9 \pm 1.3$  (–) when including the first cut. The larger difference between the ERU and  $\iota$  after the cuts  
348 reflect the higher respiration rates of the ecosystem.

349 Under low light conditions, the LRU increased during pre- and post-cut phases in a similar manner with the last 15-day  
350 period in October showing an earlier increase in the morning and evening (see Fig. S7).



351

352 **Figure 7.** (a) The seasonal cycle of  $\iota$  (black line) with the 95% confidence interval (gray area) resulting from the FP+ model and the  
 353 midday mean (11 a.m. – 2 p.m. at PAR > 800  $\mu\text{mol m}^{-2} \text{s}^{-1}$ ) ecosystem relative uptake (ERU) (blue line) using the  $\text{CO}_2$  ecosystem flux for  
 354 the calculation windows (~15 days adjusted to cuts). The dashed black line depicts the progression of the leaf area index (LAI) of the  
 355 grassland. (b) The contribution of the drivers ( $F_{\text{COS}}$ ,  $\chi_{\text{COS}}$ , GPP and  $\chi_{\text{CO}_2}$ ) to the changes in  $\iota$  between all calculation windows and the  
 356 reference period (DOY 169–188) resulting from the linear perturbation analysis compared to the observed change in  $\iota$  ( $\delta\iota$ ).

## 357 4 Discussion

### 358 4.1 Soil fluxes

359 The nighttime soil chamber measurements compare well in terms of magnitude with the COS fluxes resulting from studies  
 360 using dark chambers in agricultural and grassland sites (Whelan et al., 2018;Maseyk et al., 2014;Whelan and Rhew,  
 361 2016;Liu et al., 2010) and indicate the soil to be a small sink for COS. The current understanding of COS soil exchange links  
 362 the COS consumption to soil biota e.g. bacteria and fungi, possessing the ubiquitous enzyme CA (Kesselmeier et al.,  
 363 1999;Meredith et al., 2019). However, we also found 12 % of all nighttime fluxes to be emission. The origin of COS in soils  
 364 is still highly debated, but comparisons of untreated and sterilized soils suggest yet unknown abiotic processes (Meredith et  
 365 al., 2019;Kitz et al., 2019).

366 During daytime, the soil inside the chambers emitted COS at rates of up to 40.9  $\text{pmol m}^{-2} \text{s}^{-1}$ . These rates lie at the upper end  
 367 of recently stated values of agricultural and grassland sites (Whelan et al., 2018;Kitz et al., 2017;Maseyk et al., 2014;Liu et  
 368 al., 2010). Partly, this can be attributed to the type of chambers we used and their deployment. We allowed the full spectrum  
 369 of incoming radiation to reach the soils surface, whereas most other studies used dark chambers. Therefore we were able to  
 370 capture the influence of COS emission processes coupled to thermo- and photo production on our COS soil fluxes (Whelan  
 371 and Rhew, 2015;Kitz et al., 2019;Meredith et al., 2018). This also led to lower peak soil emissions of COS at the end of the  
 372 season, when the incoming radiation declined. Our modelled COS soil fluxes peak at about 12% of the maximum emissions  
 373 retrieved from the soil chambers. This is owed to the difference in incident radiation reaching the soil surface between the  
 374 fluxes resulting from chamber measurements and our model. For the chambers, the aboveground biomass was removed,  
 375 whereas our modelled fluxes were adjusted for undisturbed canopy conditions. In the gradient mixing ratio data, during pre-  
 376 cut conditions, we also did not see an increase in COS mixing ratio within the canopy, which would have been a hint for a  
 377 soil COS source.



378 Another factor contributing to the high COS soil emissions might be the yearly fertilization using slurry, as high nitrogen  
379 content in soils has been linked to a higher source strength of COS (Kaisermann et al., 2018). This agrees well with the study  
380 of Kitz et al. (2019), who found a correlation between increased soil nitrogen content and soil COS emission in a laboratory  
381 experiment with samples taken from the grassland at two different dates (i.e. June and September).

382 **4.2 Ecosystem fluxes**

383 Our observations show that the agriculturally used grassland acted as a major sink for COS during the growing season. The  
384 fluxes fit well within or even exceeded the COS uptake rates of published grassland and agricultural sites during their  
385 growing phases (Billesbach et al., 2014; Whelan and Rhew, 2016; Geng and Mu, 2004). The late snow event that occurred in  
386 the peak growing season almost completely inhibited the exchange of CO<sub>2</sub> and COS, as the snow acted as a diffusion barrier  
387 for these compounds (Björkman et al., 2010).

388 The cuttings and the consecutive drying of the above ground plant material at the site had a major influence on the COS  
389 exchange. During these events the grassland turned into a source for CO<sub>2</sub> and COS. This has also been reported at  
390 agricultural fields in phases of senescence (Maseyk et al., 2014; Billesbach et al., 2014). Although the soil was a strong  
391 source for COS, caused by the high R<sub>soil</sub> and T<sub>soil</sub> (Whelan and Rhew, 2015; Kitz et al., 2019; Meredith et al., 2018), and the  
392 sink strength of the grassland was low due to the reduced aboveground biomass, soil fluxes did not explain the emission on  
393 ecosystem level (see Fig. 5a). As plants contain precursors involved in COS emission processes, e.g. methionine and  
394 cysteine (Meredith et al., 2018), the plant litter and dying plant parts remaining at the site after the cuts might be the missing  
395 source of COS. Laboratory tests of the soil of the grassland have shown that a mixing of dried litter and soil lead to a strong  
396 but short-lived emission peak of COS (Kitz et al., 2019). Alternatively, the cutting of the grassland might induce stress  
397 mediated COS production in the remaining living plant parts (Bloem et al., 2012; Gimeno et al., 2017). The delay in the peak  
398 COS emissions at ecosystem scale after the cuts could indicate that some yet unknown biotic or abiotic processes take  
399 several days to release COS.

400 We also observed another COS emission event shortly after the fertilization of the grassland towards the end of the growing  
401 season. The increase of available nitrogen (Kaisermann et al., 2018) and COS precursors introduced to the soil in the form of  
402 cattle slurry (Hörtnagl et al., 2018) might have triggered the COS emission by biotic or abiotic processes.

403 Due to the independence of CA to catalyze COS without R<sub>PAR</sub> (Stimler et al., 2011), the grassland remained a sink for COS  
404 during nighttime. Again, the soil sink was too small to explain the total COS exchange (Fig. 5), which indicates that the plant  
405 stomata were not fully closed (Kooijmans et al., 2017) and were responsible for the majority of the COS uptake. The  
406 minimum or residual stomatal conductances at the field site in Neustift have been reported to be between 10 and 65 mmol m<sup>-2</sup> s<sup>-1</sup>  
407 depending on the species (Wohlfahrt, 2004).

408 Although we observed phases of high VPD and low SWC (Fig. 1), they did not lead to a decrease in CO<sub>2</sub> and COS  
409 ecosystem fluxes (Fig. S1-S2), which has already been observed for the grasslands CO<sub>2</sub> and H<sub>2</sub>O fluxes between 2001 and  
410 2009. The species located at the site were insensitive to progressive drought conditions (Brilli et al., 2011).

411 **4.3 COS mixing ratios**

412 The continuous decrease in above-canopy  $\chi_{\text{cos}}$  from ~500 ppt (in May) to ~400 ppt (in October) is within the range of  
413 published records observing mixing ratios to decrease from 465 (in summer) to 375 ppt (in winter) (Kuhn et al., 1999). This  
414 pattern is typical for the northern hemisphere and the COS drawdown by terrestrial ecosystems (Montzka et al., 2007). We  
415 found the lowest  $\chi_{\text{cos}}$  at the end of September, which coincides with the lowest ambient mixing ratios of COS, measured in  
416 Ireland, the closest COS observation site Mace Head (MHD) of NOAA, on the 6<sup>th</sup> of October.

417 Gradient observations of the diurnal cycle revealed a continuous decrease of  $\chi_{\text{cos}}$  from the atmosphere (> 500 ppt) down to  
418 the soil reaching very low concentrations of 134 ppt during nighttime. Low values like this have also been reported by



419 Rastogi et al. (2018), who measured a mean  $\chi_{\text{COS}}$  minimum of 152 ppt at 1 m above the soil within an old growth forest. The  
420 difference in concentrations during day and nighttime originates from changes in the height of the planetary boundary layer  
421 (PBL). While the PBL is shallow during nighttime and the COS mixing ratio decreases due to sink strength of the grassland,  
422 at the onset of the day, the PBL layer height increases fast and COS rich air is transported down to the ecosystem. Even  
423 though CO<sub>2</sub> and COS share a similar pathway into plants, reflected by their respective decrease in the mixing ratios within  
424 the canopy, we saw a difference at the lower levels of our gradient analysis. We only observed an increase in CO<sub>2</sub> mixing  
425 ratios, caused by the release of CO<sub>2</sub> through respiration processes in the soil, whereas COS mixing ratios further declined  
426 down to the soil surface. This supports our soil model, which predicted only minor COS fluxes under conditions of high  
427 LAI, when only a small portion of incident radiation was hitting the soil surface.

#### 428 **4.4 LRU**

429 The parameter  $\tau$  varied between 0.9 (0.8-1.0) (-) and 1.5 (1.2-1.8) (-) during the campaign, where cuts of the grassland tended  
430 to result in higher values and places this study at the lower end of a recent compilation of all published leaf-level LRUs, that  
431 put 95% of all data between 0.7 (-) and 6.2 (-) with a median of 1.7 (-) (Whelan et al., 2018) and also lower than the LRU of  
432 2.53 (-) estimated for grasslands by Seibt et al. (2010). The seasonal trend of the LRUs was strongly influenced by the  
433 cutting of the grass and can be attributed mainly to changes in the ratio of COS uptake to GPP. However, we also observed a  
434 strong decline in the ambient mixing ratio of COS, which also had an equally strong influence on the change in  $\tau$  as the COS  
435 flux for the 15 day window before the last cut (Fig 7 b).  
436 Even though the changes in  $\tau$  can be explained, it is important to keep in mind that the grassland was a source for COS on  
437 ecosystem level after the cuts. For the calculation of LRUs we had to remove those observations from the data since they  
438 would yield negative values (see Eq.8). This indicates that the unknown source strength after cuts likely decreases the post-  
439 cut  $\tau$ 's.

#### 440 **5 Conclusion**

441 Due to the management interventions at the grassland site, the leaf area development was decoupled from seasonal changes  
442 in environmental forcing. This allowed us to measure concurrent CO<sub>2</sub> and COS fluxes at soil and ecosystem level for  
443 multiple growing periods within one season. The LAI on seasonal scale as well as incoming solar radiation on hourly to  
444 seasonal scales determined whether soils were a source or a sink for COS. The incoming shortwave radiation reaching the  
445 soil surface had a decisive influence on the COS soil surface flux and thus supports our hypothesis H4. The covariance  
446 between the daytime CO<sub>2</sub> and COS fluxes on daily to seasonal level was high and the fluxes only diverged after the cuts,  
447 leading to higher LRUs. Beside the perturbations of the ecosystem, the sink strength of the grassland was high for COS and  
448 declined over the course of the season (H1). The COS emissions at ecosystem scale shortly after the cuts, which could not be  
449 explained by the soil source, raise questions about other unknown mechanisms of COS production within ecosystems (H2).  
450 With the exception of short periods after the cuts, the LRUs under high light conditions were relatively constant during the  
451 season, indicating a good correlation between the COS flux and GPP under stable conditions (H3).

#### 452 **6. Data availability**

453 Data and materials availability: Will be uploaded to <https://zenodo.org/>.  
454



455 **7. Author contributions**

456 Felix M. Spielmann: Data curation, Formal analysis, Investigation, Methodology, Software, Visualization, Writing – original  
457 draft  
458 Albin Hammerle: Data curation, Investigation, Software, Writing – original draft  
459 Florian Kitz: Data curation, Formal analysis, Investigation, Methodology, Software, Writing – original draft  
460 Katharina Gerdel: Investigation, Software, Writing – original draft  
461 Georg Wohlfahrt: Conceptualization, Funding acquisition, Investigation, Methodology, Project administration, Software,  
462 Supervision, Writing – original draft

463 **8. Competing interests**

464 The authors declare no competing financial interests.

465 **9. Acknowledgements**

466 This study was financially supported by the Austrian National Science Fund (FWF; contracts P26931, P27176, and I03859),  
467 the Tyrolean Science Fund (contract UNI-0404/1801), and the University of Innsbruck (Infrastructure funding by Research  
468 Area Alpine Space-Man and Environment to G. W). Financial support to F. M. S. was provided through a PhD scholarship  
469 by the University of Innsbruck. We thank family Hofer (Neustift, Austria) for kindly granting us access to the study site.  
470 COS flask data were provided by the Global Monitoring Division of the National Oceanic and Atmospheric  
471 Administration's Earth System Research Laboratory (NOAA ESRL/GMD). The authors declare no competing financial  
472 interests.

473 **10. References**

- 474 Asaf, D., Rotenberg, E., Tatarinov, F., Dicken, U., Montzka, S. A., and Yakir, D.: Ecosystem photosynthesis inferred from  
475 measurements of carbonyl sulphide flux, *Nature Geoscience*, 6, 186–190, 10.1038/ngeo1730, 2013.  
476 Aubinet, M., Grelle, A., Ibrom, A., Rannik, Ü., Moncrieff, J., Foken, T., Kowalski, A. S., Martin, P. H., Berbigier, P.,  
477 Bernhofer, C., Clement, R., Elbers, J., Granier, A., Grünwald, T., Morgenstern, K., Pilegaard, K., Rebmann, C.,  
478 Snijders, W., Valentini, R., and Vesala, T.: Estimates of the Annual Net Carbon and Water Exchange of Forests:  
479 The EUROFLUX Methodology, in: *Advances in Ecological Research Volume 30*, edited by: Fitter, A. H., and  
480 Raffaelli, D. G., *Advances in Ecological Research*, Academic Press, 113–175, 1999.  
481 Baldocchi, D.: Measuring fluxes of trace gases and energy between ecosystems and the atmosphere - the state and future of  
482 the eddy covariance method, *Glob Chang Biol*, 20, 3600–3609, <https://doi.org/10.1111/gcb.12649>, 2014.  
483 Billesbach, D. P., Berry, J. A., Seibt, U., Maseyk, K., Torn, M. S., Fischer, M. L., Abu-Naser, M., and Campbell, J. E.:  
484 Growing season eddy covariance measurements of carbonyl sulfide and CO<sub>2</sub> fluxes: COS and CO<sub>2</sub> relationships in  
485 Southern Great Plains winter wheat, *Agricultural and Forest Meteorology*, 184, 48–55,  
486 10.1016/j.agrformet.2013.06.007, 2014.  
487 Björkman, M. P., Morgner, E., Cooper, E. J., Elberling, B., Klemedtsson, L., and Björk, R. G.: Winter carbon dioxide  
488 effluxes from Arctic ecosystems: An overview and comparison of methodologies, *Global Biogeochemical Cycles*,  
489 24, 10.1029/2009gb003667, 2010.  
490 Bloem, E., Haneklaus, S., Kesselmeier, J., and Schnug, E.: Sulfur Fertilization and Fungal Infections Affect the Exchange of  
491 H<sub>2</sub>S and COS from Agricultural Crops, *Journal of Agricultural and Food Chemistry*, 60, 7588–7596,  
492 10.1021/jf301912h, 2012.  
493 Brilli, F., Hörtagl, L., Hammerle, A., Haswanter, A., Hansel, A., Loreto, F., and Wohlfahrt, G.: Leaf and ecosystem  
494 response to soil water availability in mountain grasslands, *Agricultural and Forest Meteorology*, 151, 1731–1740,  
495 <https://doi.org/10.1016/j.agrformet.2011.07.007>, 2011.  
496 Brühl, C., Lelieveld, J., Crutzen, P. J., and Tost, H.: The role of carbonyl sulphide as a source of stratospheric sulphate  
497 aerosol and its impact on climate, *Atmos. Chem. Phys.*, 12, 1239–1253, 10.5194/acp-12-1239-2012, 2012.  
498 Ensign, S. A.: Reactivity of Carbon Monoxide Dehydrogenase from Rhodospirillum rubrum with Carbon Dioxide, Carbonyl  
499 Sulfide, and Carbon Disulfide, *Biochemistry*, 34, 5372–5381, 10.1021/bi00016a008, 1995.  
500 Geng, C., and Mu, Y.: Carbonyl sulfide and dimethyl sulfide exchange between lawn and the atmosphere, *Journal of  
501 Geophysical Research: Atmospheres*, 109, 10.1029/2003jd004492, 2004.



- 502 Gerdel, K., Spielmann, F. M., Hammerle, A., and Wohlfahrt, G.: Eddy covariance carbonyl sulfide flux measurements with a  
503 quantum cascade laser absorption spectrometer, *Atmospheric Measurement Techniques*, 10, 3525-3537,  
504 10.5194/amt-10-3525-2017, 2017.
- 505 Gimeno, T. E., Ogee, J., Royles, J., Gibon, Y., West, J. B., Burlett, R., Jones, S. P., Sauze, J., Wohl, S., Benard, C., Genty,  
506 B., and Wingate, L.: Bryophyte gas-exchange dynamics along varying hydration status reveal a significant carbonyl  
507 sulphide (COS) sink in the dark and COS source in the light, *New Phytologist*, 215, 965-976, 10.1111/nph.14584,  
508 2017.
- 509 Hortnagl, L., Clement, R., Graus, M., Hammerle, A., Hansel, A., and Wohlfahrt, G.: Dealing with disjunct concentration  
510 measurements in eddy covariance applications: A comparison of available approaches, *Atmospheric Environment*,  
511 44, 2024-2032, 10.1016/j.atmosenv.2010.02.042, 2010.
- 512 Hörtnagl, L., Barthel, M., Buchmann, N., Eugster, W., Butterbach-Bahl, K., Díaz-Pinés, E., Zeeman, M., Klumpp, K., Kiese,  
513 R., Bahn, M., Hammerle, A., Lu, H., Ladreiter-Knauss, T., Burri, S., and Merbold, L.: Greenhouse gas fluxes over  
514 managed grasslands in Central Europe, *Global Change Biology*, 24, 1843-1872, 10.1111/gcb.14079, 2018.
- 515 Kaisermann, A., Jones, S., Wohl, S., Ogée, J., and Wingate, L.: Nitrogen Fertilization Reduces the Capacity of Soils to Take  
516 up Atmospheric Carbonyl Sulphide, *Soil Syst.*, 2, 10.3390/soilsystems2040062, 2018.
- 517 Kesselmeier, J., Teusch, N., and Kuhn, U.: Controlling variables for the uptake of atmospheric carbonyl sulfide by soil, *J.  
518 Geophys. Res.-Atmos.*, 104, 11577-11584, 10.1029/1999jd900090, 1999.
- 519 Kitz, F., Gerdel, K., Hammerle, A., Laterza, T., Spielmann, F. M., and Wohlfahrt, G.: In situ soil COS exchange of a  
520 temperate mountain grassland under simulated drought, *Oecologia*, 1-10, 10.1007/s00442-016-3805-0, 2017.
- 521 Kitz, F., Gómez-Brandón, M., Eder, B., Etemadi, M., Spielmann, F. M., Hammerle, A., Insam, H., and Wohlfahrt, G.: Soil  
522 carbonyl sulfide exchange in relation to microbial community composition: Insights from a managed grassland soil  
523 amendment experiment, *Soil Biology and Biochemistry*, 135, 28-37, 10.1016/j.soilbio.2019.04.005, 2019.
- 524 Kooijmans, L. M. J., Uitlag, N. A. M., Zahniser, M. S., Nelson, D. D., Montzka, S. A., and Chen, H. L.: Continuous and  
525 high-precision atmospheric concentration measurements of COS, CO<sub>2</sub>, CO and H<sub>2</sub>O using a quantum cascade laser  
526 spectrometer (QCLS), *Atmospheric Measurement Techniques*, 9, 5293-5314, 10.5194/amt-9-5293-2016, 2016.
- 527 Kooijmans, L. M. J., Maseyk, K., Seibt, U., Sun, W., Vesala, T., Mammarella, I., Kolaric, P., Aalto, J., Franchin, A., Vecchi,  
528 R., Valli, G., and Chen, H.: Canopy uptake dominates nighttime carbonyl sulfide fluxes in a boreal forest, *Atmos.  
529 Chem. Phys.*, 17, 11453-11465, 10.5194/acp-17-11453-2017, 2017.
- 530 Kooijmans, L. M. J., Sun, W., Aalto, J., Erkkilä, K. M., Maseyk, K., Seibt, U., Vesala, T., Mammarella, I., and Chen, H.:  
531 Influences of light and humidity on carbonyl sulfide-based estimates of photosynthesis, *Proc Natl Acad Sci U S A*,  
532 10.1073/pnas.1807600116, 2019.
- 533 Krysztofiak, G., Té, Y. V., Catoire, V., Berthet, G., Toon, G. C., Jégou, F., Jeseck, P., and Robert, C.: Carbonyl Sulphide  
534 (OCS) Variability with Latitude in the Atmosphere, *Atmosphere-Ocean*, 53, 89-101,  
535 10.1080/07055900.2013.876609, 2015.
- 536 Kuhn, U., Ammann, C., Wolf, A., Meixner, F. X., Andreae, M. O., and Kesselmeier, J.: Carbonyl sulfide exchange on an  
537 ecosystem scale: soil represents a dominant sink for atmospheric COS, *Atmospheric Environment*, 33, 995-1008,  
538 Doi 10.1016/S1352-2310(98)00211-8, 1999.
- 539 Langford, B., Acton, W., Ammann, C., Valach, A., and Nemitz, E.: Eddy-covariance data with low signal-to-noise ratio:  
540 time-lag determination, uncertainties and limit of detection, *Atmospheric Measurement Techniques*, 8, 4197-4213,  
541 10.5194/amt-8-4197-2015, 2015.
- 542 Lasslop, G., Reichstein, M., Papale, D., Richardson, A. D., Arneth, A., Barr, A., Stoy, P., and Wohlfahrt, G.: Separation of  
543 net ecosystem exchange into assimilation and respiration using a light response curve approach: critical issues and  
544 global evaluation, *Global Change Biology*, 16, 187-208, 10.1111/j.1365-2486.2009.02041.x, 2010.
- 545 Le Quere, C., Andrew, R. M., Friedlingstein, P., Sitch, S., Pongratz, J., Manning, A. C., Korsbakken, J. I., Peters, G. P.,  
546 Canadell, J. G., Jackson, R. B., Boden, T. A., Tans, P. P., Andrews, O. D., Arora, V. K., Bakker, D. C. E., Barbero,  
547 L., Becker, M., Betts, R. A., Bopp, L., Chevallier, F., Chini, L. P., Ciais, P., Cosca, C. E., Cross, J., Currie, K.,  
548 Gasser, T., Harris, I., Hauck, J., Haverd, V., Houghton, R. A., Hunt, C. W., Hurtt, G., Ilyina, T., Jain, A. K., Kato,  
549 E., Kautz, M., Keeling, R. F., Goldewijk, K. K., Kortzinger, A., Landschutzer, P., Lefevre, N., Lenton, A., Lienert,  
550 S., Lima, I., Lombardozzi, D., Metzl, N., Millero, F., Monteiro, P. M. S., Munro, D. R., Nabel, J., Nakaoka, S.,  
551 Nojiri, Y., Padin, X. A., Peregon, A., Pfeil, B., Pierrot, D., Poulet, B., Rehder, G., Reimer, J., Rodenbeck, C.,  
552 Schwinger, J., Seferian, R., Skjelvan, I., Stocker, B. D., Tian, H. Q., Tilbrook, B., Tubiello, F. N., van der Laan-  
553 Luijkx, I. T., van der Werf, G. R., van Heuven, S., Viovy, N., Vuichard, N., Walker, A. P., Watson, A. J., Wiltshire,  
554 A. J., Zaehle, S., and Zhu, D.: Global Carbon Budget 2017, *Earth System Science Data*, 10, 405-448, 10.5194/essd-  
555 10-405-2018, 2018.
- 556 Liaw, A., and Wiener, M.: Classification and Regression by RandomForest, *R News*, 2/3, 18-22, 2002.
- 557 Liu, J., Geng, C., Mu, Y., Zhang, Y., Xu, Z., and Wu, H.: Exchange of carbonyl sulfide (COS) between the atmosphere and  
558 various soils in China, *Biogeosciences*, 7, 753-762, 10.5194/bg-7-753-2010, 2010.
- 559 Lorimer, G. H., and Pierce, J.: Carbonyl sulfide: an alternate substrate for but not an activator of ribulose-1,5-bisphosphate  
560 carboxylase, *The Journal of biological chemistry*, 264, 2764-2772, 1989.
- 561 Maseyk, K., Berry, J. A., Billesbach, D., Campbell, J. E., Torn, M. S., Zahniser, M., and Seibt, U.: Sources and sinks of  
562 carbonyl sulfide in an agricultural field in the Southern Great Plains, *Proceedings of the National Academy of  
563 Sciences of the United States of America*, 111, 9064-9069, 10.1073/pnas.1319132111, 2014.
- 564 Meredith, L. K., Boye, K., Youngerman, C., Whelan, M., Ogee, J., Sauze, J., and Wingate, L.: Coupled Biological and  
565 Abiotic Mechanisms Driving Carbonyl Sulfide Production in Soils, *Soil Syst.*, 2, 27, ARTN 37



- 566 10.3390/soilsystems2030037, 2018.  
567 Meredith, L. K., Ogée, J., Boye, K., Singer, E., Wingate, L., von Sperber, C., Sengupta, A., Whelan, M., Pang, E., Keiluweit,  
568 M., Brüggemann, N., Berry, J. A., and Welander, P. V.: Soil exchange rates of COS and CO<sub>18</sub>O differ with the  
569 diversity of microbial communities and their carbonic anhydrase enzymes, *The ISME Journal*, 13, 290-300,  
570 10.1038/s41396-018-0270-2, 2019.  
571 Montzka, S. A., Calvert, P., Hall, B. D., Elkins, J. W., Conway, T. J., Tans, P. P., and Sweeney, C.: On the global  
572 distribution, seasonality, and budget of atmospheric carbonyl sulfide (COS) and some similarities to CO<sub>2</sub>, *J. Geophys. Res.-Atmos.*, 112, 10.1029/2006jd007665, 2007.  
573 Notni, J., Schenk, S., Protoschill-Krebs, G., Kesselmeier, J., and Anders, E.: The missing link in COS metabolism: a model  
574 study on the reactivation of carbonic anhydrase from its hydrosulfide analogue, *Chembiochem : a European journal*  
575 of chemical biology
- 576 8, 530-536, 10.1002/cbic.200600436, 2007.  
577 Ogawa, T., Noguchi, K., Saito, M., Nagahata, Y., Kato, H., Ohtaki, A., Nakayama, H., Dohmae, N., Matsushita, Y., Odaka,  
578 M., Yohda, M., Nyunoya, H., and Katayama, Y.: Carbonyl Sulfide Hydrolase from *Thiobacillus thioparus* Strain  
579 THI115 Is One of the β-Carbonic Anhydrase Family Enzymes, *Journal of the American Chemical Society*, 135,  
580 3818-3825, 10.1021/ja307735e, 2013.  
581 Protoschill-Krebs, G., and Kesselmeier, J.: ENZYMATIC PATHWAYS FOR THE CONSUMPTION OF CARBONYL  
582 SULFIDE (COS) BY HIGHER-PLANTS, *Botanica Acta*, 105, 206-212, 1992.  
583 Rastogi, B., Berkelhammer, M., Wharton, S., Whelan, M. E., Itter, M. S., Leen, J. B., Gupta, M. X., Noone, D., and Still, C.  
584 J.: Large Uptake of Atmospheric OCS Observed at a Moist Old Growth Forest: Controls and Implications for  
585 Carbon Cycle Applications, *Journal of Geophysical Research-Biogeosciences*, 123, 3424-3438,  
586 10.1029/2018jg004430, 2018.  
587 Sandoval-Soto, L., Stanimirov, M., von Hobe, M., Schmitt, V., Valdes, J., Wild, A., and Kesselmeier, J.: Global uptake of  
588 carbonyl sulfide (COS) by terrestrial vegetation: Estimates corrected by deposition velocities normalized to the  
589 uptake of carbon dioxide (CO<sub>2</sub>), *Biogeosciences*, 2, 125-132, 10.5194/bg-2-125-2005, 2005.  
590 Seefeldt, L. C., Rasche, M. E., and Ensign, S. A.: Carbonyl sulfide and carbon dioxide as new substrates, and carbon  
591 disulfide as a new inhibitor, of nitrogenase, *Biochemistry*, 34, 5382-5389, 10.1021/bi00016a009, 1995.  
592 Seibt, U., Kesselmeier, J., Sandoval-Soto, L., Kuhn, U., and Berry, J.: A kinetic analysis of leaf uptake of COS and its  
593 relation to transpiration, photosynthesis and carbon isotope fractionation, *Biogeosciences*, 7, 333-341, 2010.  
594 Smeulders, M. J., Pol, A., Venselaar, H., Barends, T. R. M., Hermans, J., Jetten, M. S. M., and Op den Camp, H. J. M.:  
595 Bacterial CS<sub>2</sub> Hydrolases from <span class="named-content genus-species" id="named-content-1">Acidithiobacillus thiooxidans</span> Strains Are Homologous to the  
596 Archaeal Catenate CS<sub>2</sub> Hydrolase, *Journal of Bacteriology*, 195, 4046, 10.1128/JB.00627-13, 2013.  
597 Spielmann, F. M., Wohlfahrt, G., Hammerle, A., Kitz, F., Migliavacca, M., Alberti, G., Ibrom, A., El-Madany, T. S., Gerdel,  
598 K., Moreno, G., Kolle, O., Karl, T., Peressotti, A., and Delle Vedove, G.: Gross Primary Productivity of Four  
599 European Ecosystems Constrained by Joint CO<sub>2</sub> and COS Flux Measurements, *Geophys. Res. Lett.*, 0,  
600 10.1029/2019gl082006, 2019.  
601 Stimler, K., Berry, J. A., Montzka, S. A., and Yakir, D.: Association between Carbonyl Sulfide Uptake and (18)Delta during  
602 Gas Exchange in C-3 and C-4 Leaves, *Plant Physiology*, 157, 509-517, 10.1104/pp.111.176578, 2011.  
603 Stoy, P. C., Katul, G. G., Siqueira, M. B. S., Juang, J. Y., Novick, K. A., McCarthy, H. R., Oishi, A. C., Uebelherr, J. M.,  
604 Kim, H. S., and Oren, R.: Separating the effects of climate and vegetation on evapotranspiration along a  
605 successional chronosequence in the southeastern US, *Global Change Biology*, 12, 2115-2135, 10.1111/j.1365-  
606 2486.2006.01244.x, 2006.  
607 Whelan, M. E., and Rhew, R. C.: Carbonyl sulfide produced by abiotic thermal and photodegradation of soil organic matter  
608 from wheat field substrate, *Journal of Geophysical Research-Biogeosciences*, 120, 54-62, 10.1002/2014jg002661,  
609 2015.  
610 Whelan, M. E., and Rhew, R. C.: Reduced sulfur trace gas exchange between a seasonally dry grassland and the atmosphere,  
611 *Biogeochemistry*, 128, 267-280, 10.1007/s10533-016-0207-7, 2016.  
612 Whelan, M. E., Lennartz, S. T., Gimeno, T. E., Wehr, R., Wohlfahrt, G., Wang, Y., Kooijmans, L. M. J., Hilton, T. W.,  
613 Belviso, S., Peylin, P., Commane, R., Sun, W., Chen, H., Kuai, L., Mammarella, I., Maseyk, K., Berkelhammer, M.,  
614 Li, K. F., Yakir, D., Zumkehr, A., Katayama, Y., Ogée, J., Spielmann, F. M., Kitz, F., Rastogi, B., Kesselmeier, J.,  
615 Marshall, J., Erkkilä, K. M., Wingate, L., Meredith, L. K., He, W., Bunk, R., Launois, T., Vesala, T., Schmidt, J. A.,  
616 Fichot, C. G., Seibt, U., Saleska, S., Saltzman, E. S., Montzka, S. A., Berry, J. A., and Campbell, J. E.: Reviews and  
617 syntheses: Carbonyl sulfide as a multi-scale tracer for carbon and water cycles, *Biogeosciences*, 15, 3625-3657,  
618 10.5194/bg-15-3625-2018, 2018.  
619 Wohlfahrt, G., Bahn, M., Tappeiner, U., and Cernusca, A.: A multi-component, multi-species model of vegetation-  
620 atmosphere CO<sub>2</sub> and energy exchange for mountain grasslands, *Agricultural and Forest Meteorology*, 106, 261-  
621 287, 10.1016/s0168-1923(00)00224-0, 2001.  
622 Wohlfahrt, G.: Modelling fluxes and concentrations of CO<sub>2</sub>, H<sub>2</sub>O and sensible heat within and above a mountain meadow  
623 canopy: A comparison of three Lagrangian models and three parameterisation options for the Lagrangian time  
624 scale, *Boundary-Layer Meteorology*, 113, 43-80, 10.1023/B:BOUN.0000037326.40490.1f, 2004.  
625 Wohlfahrt, G., Hammerle, A., Haslwanter, A., Bahn, M., Tappeiner, U., and Cernusca, A.: Seasonal and inter-annual  
626 variability of the net ecosystem CO<sub>2</sub> exchange of a temperate mountain grassland: Effects of weather and  
627 management, *Journal of Geophysical Research: Atmospheres*, 113, 10.1029/2007jd009286, 2008.  
628



- 630 Wohlfahrt, G., Brilli, F., Hoertnagl, L., Xu, X., Bingemer, H., Hansel, A., and Loreto, F.: Carbonyl sulfide (COS) as a tracer  
631 for canopy photosynthesis, transpiration and stomatal conductance: potential and limitations, *Plant Cell and*  
632 *Environment*, 35, 657-667, 10.1111/j.1365-3040.2011.02451.x, 2012.  
633 Yang, F., Qubaja, R., Tatarinov, F., Rotenberg, E., and Yakir, D.: Assessing canopy performance using carbonyl sulfide  
634 measurements, *Global Change Biology*, 24, 3486-3498, doi:10.1111/gcb.14145, 2018.  
635